Explanation of edge defect influence on sapphire bending strength scatter using the coupled criterion

Aurélien Doitrand, Ronan Henry, Sylvain Meille

Explanation of edge defect influence on sapphire bending strength scatter using the coupled criterion

Aurelien Doitrand[1], Ronan Henry[2], and Sylvain Meille[1]

[1] Univ Lyon, INSA Lyon, Université Claude Bernard Lyon 1, CNRS UMR5510, MATEIS, F-69621 Villeurbanne, France, aurelien.doitrand@insa-lyon.fr
[2] CNRS, Univ Rouen Normandie, INSA Rouen Normandie, Normandie Univ, GPM UMR 6634, F-76000 Rouen, France

Sapphire fracture is studied by means of four-point bending tests on mirror-polished millimetric specimens having their cristallographic $\vec{a}$-axis oriented along the specimen length. The scattering of bending strengths between 500 MPa and 750 MPa is mainly due to edge defects of some tens of microns resulting from the specimen cutting process. Crack initiation occurs from an edge defect along a a-plane, perpendicular to the direction of maximum tensile stress, and further deviates along weaker m-planes. Numerical simulations of edge defect-induced crack initiation based on the coupled criterion reveal that the material sensitivity to edge defect-induced crack initiation mainly depends on Irwin's length. For Irwin's lengths larger than twice the defect depth, the bending strength is the same as the one obtained without defect. By retrieving the bending strength variation as a function of the defect depth measured experimentally, the proposed approach enables the identification of sapphire a-plane 850 ± 90 MPa tensile strength for a $\mathcal{G}_c = 15\,\mathrm{J\,m^{-2}}$ critical energy release rate.

Keywords Sapphire, failure, defects, coupled criterion, tensile strength

1 Introduction

Brittle fracture is common in ceramics, it is usually explained by the presence of defects within the microstructure, which locally weaken the material and lead to its fracture. One way to estimate the critical defect size from the measured fracture stress σ_R is to use the energy criterion defined in the framework of linear elastic fracture mechanics (LEFM) (Griffith 1921; Griffith 1924). Irwin's approach (Irwin 1957; Irwin 1958; McClintock et al. 1965) gives the critical crack size $a_c = \frac{K_{Ic}^2}{\pi\sigma_R^2}$ that propagates under such a remote tensile stress σ_R as a function of the material critical stress intensity factor K_{Ic} . However, it should be noted that this approach is only applicable under the assumption of a crack subjected to uniform tension in an infinite medium. It thus cannot assess configurations other than a sufficiently long pre-existing crack. The approach is valid provided the pre-existing crack length is larger than the Irwin's length, which is a characteristic of the material defined as $\ell_{mat} = \frac{E\mathcal{G}_c}{(1-\nu^2)\sigma_c^2}$, where E is the material Young's modulus, ν the material Poisson's ration, $\mathcal{G}_c$ its critical energy release rate and σ_c its tensile strength. The Irwin's length is often compared to the size of the fracture process zone, which represents a region near the crack tip where nonlinear phenomena, such as damage or plasticity, occurs. The fracture process zone is present even in brittle materials (Irwin 1948; Orowan 1949), which explains why the true critical energy release rate is several orders of magnitude larger than the surface energy density originally proposed by Griffith. Irwin's length is crucial in fracture mechanics as it is related to the initiation length in the coupled criterion (Leguillon 2002; Doitrand et al. 2020c), it defines the regularization length in phase-field fracture models (Molnár et al. 2020), and it is related to the critical displacement jump and the process zone extent in cohesive zone models (Barenblatt 1959; Dugdale 1960). It is also used as an input for non-local stress evaluation in the theory of critical distances (Taylor 2007). The application of Irwin's approach to evaluate a critical defect size in a ceramic neglects both the location of the crack within the specimen and the actual shape of the defect (a porosity would then be assimilated to a crack if this approach is used).

The criticality of a defect can be evaluated by studying the phenomenon of crack initiation from the defect. However, when studying a more general defect shape than a crack such as, *e.g.,* a V-notch (Leguillon et al. 1987; Dunn et al. 1997; Yosibash et al. 2006), a U-notch (Nishida et al.

1994; Picard et al. 2006; Sapora et al. 2021), or a pore (Li et al. 2006; Leguillon et al. 2006; Martin et al. 2012; Romani et al. 2015), the sole use of an energy criterion is not sufficient as the energy release rate tends towards zero for vanishing crack lengths (Leguillon et al. 1987; Labossiere et al. 1999). The limitation of LEFM in studying crack initiation can be overcome using the coupled criterion (CC) (Leguillon 2001; Leguillon 2002). The underlying idea of the CC is to combine the energy criterion together with a stress criterion (Leguillon 2002; Cornetti et al. 2006) to address crack initiation. Among various applications of the CC (Weißgraeber et al. 2016a; Doitrand et al. 2024), different defect configurations were studied such as circular (Rosendahl et al. 2017; Felger et al. 2017; Sapora et al. 2018; Cornetti et al. 2019; Carrère et al. 2021), spherical (Chao Correas et al. 2021; Ferrian et al. 2022) or elliptical holes (Carpinteri et al. 2012; Weißgraeber et al. 2016b). These approaches somehow generalize Irwin's approach to study the influence of the size of other defect shapes on fracture. It was also shown that not only the defect size but also its location within the specimen has a first order influence on crack initiation, both under bending (Doitrand et al. 2021a; Uhl et al. 2022) or tensile loading (Doitrand et al. 2021b).

The input fracture parameters of the CC are the material critical energy release rate $\mathcal{G}_c$ and the tensile strength σ_c. From a modeling perspective, σ_c corresponds to the strength of a sufficiently long specimen loaded under tension (Leguillon 2002; Doitrand et al. 2020a; Jiménez-Alfaro et al. 2021). Translating this definition into experimental terms is not trivial when dealing with brittle ceramics. Tensile tests are generally not performed on monolithic ceramics as they are not easy to set up and because the resulting homogeneous stress state exacerbates the sensitivity of fracture to the presence of a defect. Instead, flexural tests are typically preferred, as they induce a stress gradient and create a preferential zone for crack initiation on the tensile side of the specimen. The definition of the tensile strength for polycrystalline ceramics was established by studying the fracture of specimens with a surface defect (Leguillon et al. 2018; Martin et al. 2018). For surface defects larger than the ceramic average grain size, the fracture stress increased as the defect size decreased, following Irwin's approach provided that the defect that can be assimilated to a crack. However, for surface defects smaller than the grain size, the fracture stress reached a plateau that corresponded to the tensile strength of the ceramic. However, the tensile strength measurement were still scattered due to possible heterogeneities (such as grain size variation or internal pores) in the polycrystalline ceramic microstructure.

The objective of this work is to study sapphire fracture in order to consider the influence of edge defects and determine its tensile strength. Mechanical tests of millimetric specimens and observations of related defects are presented in Section 2. The modeling of crack initiation from a defect based on the CC is then presented in Section 3. The influence of the defect size on sapphire fracture and its tensile strength determination is finally presented in Section 4.

2 Experiments

The material under investigation is sapphire (Saint-Gobain Lumilog), which is a crystal with a hexagonal compact structure. A sapphire wafer was cut with a diamond wire saw to prepare $2.5 \times 0.8 \times 30$ mm^3 bars. One face of the sample is mirror polished. The specimen are cut so that the $\vec{a}$ direction corresponds to the bar main dimension, which means that a a-plane ($11\bar{2}0$ type) is perpendicular to the sample neutral axis. Twenty-three specimens, whose dimensions are summarized in Table 1, are tested under four-point bending using a Instron 8862 (USA) machine equipped with a 5 kN load cell at 0.1 mm/min displacement rate. A specimen before test is shown in Figure 1(a). The specimen length is 30 mm, the distance between the supports is 12 mm and the distance between the loading spans is 3 mm. The mirror-polished specimen face is the one that it is loaded under tension, so the possible presence of surface defects is mainly due to the specimen cutting step from the original disk, *i.e.,* these defects are not purposely induced in the specimens. For all specimens, a linear elastic behavior until brittle failure is recorded. The measured failure force F_c enables the specimen bending strength σ_f to be determined based on Euler-Bernoulli's beam theory. Figure 1(b) shows a specimen after testing which, at first sight, exhibits a V-shaped failure pattern. The specimen actually breaks into three parts, following two fracture paths oriented at 30 deg. from the bar cross section plane. This failure pattern is observed for all the tested specimen and the fracture planes oriented at 30 deg. correspond to sapphire m-planes

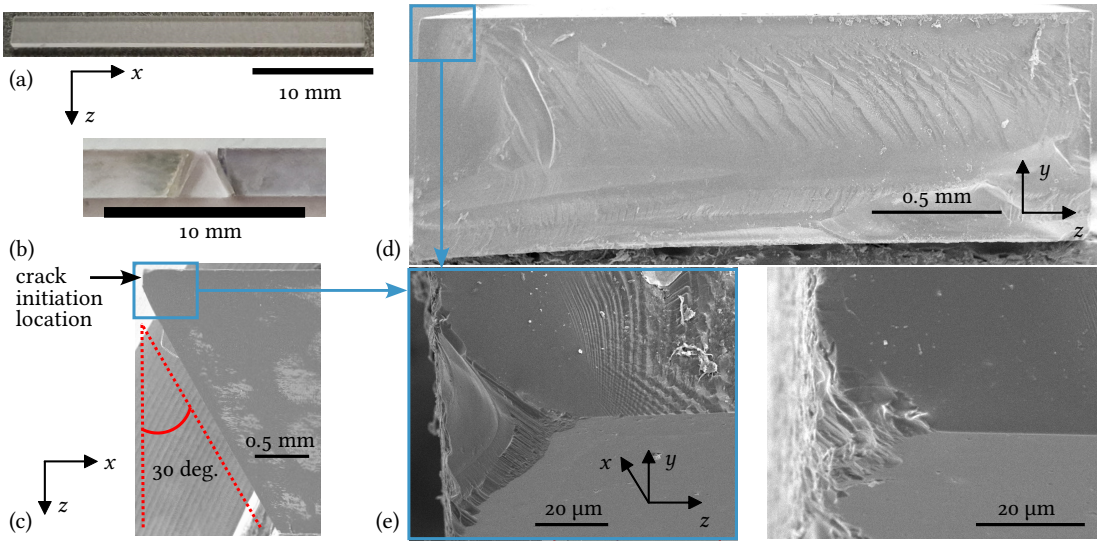

Figure 1: Optical observation of a bending specimen a) before and b) after failure. Scanning electron microscope observations of the specimen after failure c) top view, d) fracture surface view and e) focus on an edge defect located at the fracture surface (two examples of edge defect are shown).

Specimen #	B (mm)	W (mm)	F_c (N)	σ_f (MPa)	d (µm)
1	2.45	0.78	59.3	537.1	20
2	2.45	0.78	63.4	574.2	25
3	2.45	0.79	81.9	723.1	20
4	2.43	0.79	72.0	640.9	15
5	2.43	0.78	53.9	492.2	40
6	2.44	0.78	60.1	546.6	25
7	2.44	0.78	64.8	589.3	30
8	2.44	0.78	81.0	736.6	15
9	2.44	0.78	78.0	709.3	10
10	2.43	0.78	72.9	665.7	10
11	2.44	0.79	62.3	552.3	30
12	2.45	0.78	75.2	681.1	15
13	2.44	0.78	62.4	567.5	20
14	2.45	0.78	74.5	674.7	10
15	2.45	0.78	76.3	691.0	5
16	2.45	0.79	79.4	701.0	5
17	2.45	0.78	82.3	745.4	10
18	2.44	0.79	85.0	753.5	5
19	2.45	0.79	75.3	664.8	15
20	2.44	0.78	76.6	696.6	20
21	2.45	0.79	65.1	574.8	25
22	2.45	0.79	78.0	688.3	15
23	2.45	0.79	79.7	703.4	5

Table 1: Dimensions (width W and thickness B), failure force (F_c), bending strength (σ_f) and critical edge defect depth (d) measured for the tested sapphire specimens.

which are among their weakest plane (Wiederhorn 1969). Figure 1(c) shows a Scanning Electron Microscope (SEM) top view of the specimen (*i.e.,* the apparent face is the mirror-polished face). Most of the fracture surface makes a 30 deg. angle with respect to the specimen cross section, but it is observed that a part of the fracture surface is actually perpendicular to the specimen neutral

axis and thus coincide with a a-plane. As a consequence, two scenarii are possible to explain the observed fracture pattern: either crack initiation on a a-plane perpendicular to the specimen neutral axis, or crack initiation along a m-plane oriented at 30 deg.

A first possible scenario would be crack initiation along a m-plane. However, since its orientation is 30 deg. from the specimen cross section plane, it means that the local opening stress is smaller than the one acting on the cross section plane. In addition, this scenario would not explain the V-shaped fracture pattern, that is more likely to originate from crack branching after initiation. We thus conclude that crack initiation rather occurs on a a-plane perpendicular to the specimen neutral axis, on which the opening stress is the highest. This conclusion is supported by having a closer look at the fracture surfaces, that evidence the presence of defects located on the edge of the mirror-polished surface under tension (Figure 1(d-e)). A flat-like surface is observed just around the defect (Figure 1(e)), indicating a dynamic crack initiation from the defect at the specimen surface under tension. The fracture surface becomes rougher at the end of this flat zone, indicating that the crack initiated on the specimen a-plane tends to deviate to propagate along a plane with a weaker fracture energy, *i.e.,* the m-plane. This crack branching also occurs from the specimen face under tension, as evidence by a second flat-like zone indicating a dynamic crack propagation along the m-plane stemming from the surface under tension (Figure 1(d)). Once initiated from the edge defect and deviated along the m-plane from the face under tension, the end of the crack propagation is indicated by fracture surface that becomes rougher when approaching the face initially located under compression. This roughening is typical of the final ceramic specimen failure (Quinn 2020) (Figure 1(d)). The observations of all the tested specimen fracture surfaces reveal that the shape of the critical defect slightly differ depending on the specimen as shown in Figure 1(e). The defect shapes are mainly wedge-like and the defect size was measured as the largest depth either along $(O\vec{y})$ or $(O\vec{z})$ axis. The defect sizes were evaluated for all the specimens based on SEM observations and are reported in Table 1, ranging between 5 µm and 40 µm. An overall trend is observed that the lower the measured bending strengths, the deeper the edge defect.

3 Edge defect-induced fracture

3.1 The coupled criterion

Surface defect-induced crack initiation is assessed using the CC (Leguillon 2001; Leguillon 2002) in the framework of Finite Fracture Mechanics (Hashin 1996; Nairn 2000) under the assumption of small deformations and considering linear elastic material behavior. The configuration under investigation of a four-point bending specimen including an edge defect is depicted in Figure 2(a), assuming a defect shape close to the ones observed experimentally, but involving a single parameter, its depth d. Note that influence of the defect shape on the failure loading depends on the Irwin's length, since the defect morphology has a limited influence on the failure loading if it size ranges between $\ell_{\text{mat}}/10$ and $\ell_{\text{mat}}/2$ (Martin et al. 2018), and that differences up to 20 % may be obtained depending on the shape of defects larger than $\ell_{\text{mat}}/2$ (Leguillon et al. 2007; Martin et al. 2018). The objective of the CC is to determine, for a given defect depth, the imposed displacement at which a crack initiates from the defect. The underlying idea of the CC is that crack initiation occurs provided the fulfillment of both a stress criterion and an energy criterion. The energy criterion derives from the energy conservation principle (Leguillon 2002; Doitrand et al. 2020c) and writes:

$$\mathcal{G}_{\text{inc}}(S) \geqslant \mathcal{G}_{\text{c}}, \tag{1}$$

where $\mathcal{G}_{\text{inc}}$ is the incremental energy release rate (IERR) defined as $\mathcal{G}_{\text{inc}} = -\Delta\mathcal{W}_{\text{el}}/S$, *i.e.,* the ratio between the elastic strain energy ($\mathcal{W}_{\text{el}}$) variation due to crack initiation and the crack surface (S). This criterion reverts to Griffith's criterion when it is applied to study the propagation of a semi-infinite crack embedded in an infinite medium. The stress criterion is a non-local condition that must be fulfilled at all points $\boldsymbol{x}$ over the new crack path Γ before initiation:

$$\sigma_{\text{nn}}(\boldsymbol{x}) \geqslant \sigma_{\text{c}}, \forall\, \boldsymbol{x} \in \Gamma \tag{2}$$

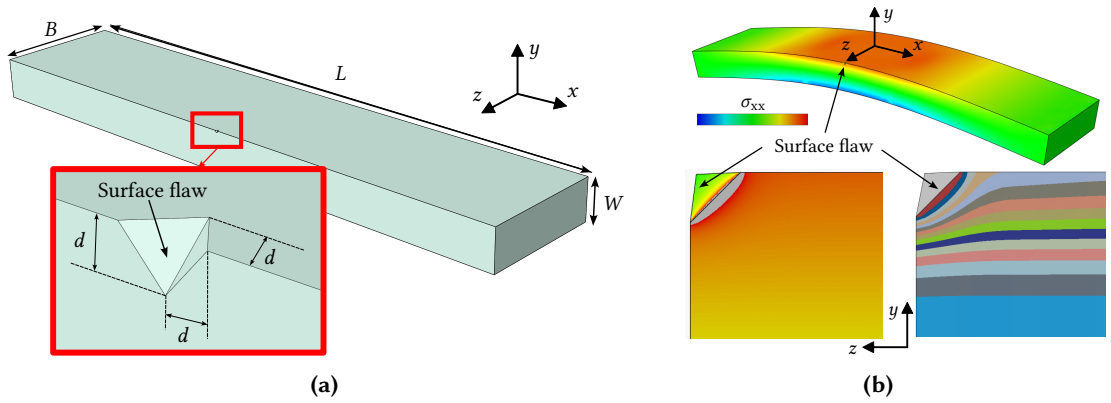

Figure 2: a) Geometry of the bending specimens under investigation including an edge defect of depth d. b) Stress field under 4-point bending and emphasis on the singular stress field around the surface flaw, based on which the potential crack surfaces are defined to further calculate the incremental energy release rate.

where σ_{nn} is the stress component normal to the crack path Γ and σ_{c} is the material tensile strength. The main difficulty when applying the CC in 3D is that the crack path Γ is a priori unknown. A first way to address this issue is to describe the crack shape by several parameters (García et al. 2016; Yosibash et al. 2016; Doitrand et al. 2017; García et al. 2018; Papšík et al. 2023; Vereecke et al. 2024; Burhan et al. 2024). Previous works showed that the alternative choice of potential crack shapes based on the stress isocontours is a reasonable assumption to accurately determine the initiation loading (Leguillon 2014; Doitrand et al. 2018; Doitrand et al. 2020b; Sevecek et al. 2019; Girard et al. 2024). The advantage of this method is that it provides a unique description $\Gamma(S)$ of the crack topology for a given crack surface. Moreover, the definition of the stress isocontours ensure that an increasing crack surface corresponds to a decreasing stress level. As a consequence, if the stress criterion is fulfilled on the crack front of $\Gamma(S)$ before initiation, it is also fulfilled anywhere inside $\Gamma(S)$. Thus, the stress criterion can unambiguously be written as a function of the crack surface:

$$\sigma_{\mathrm{nn}}(S) \geqslant \sigma_{\mathrm{c}}. \tag{3}$$

Under the assumptions of linear elasticity and small deformations, the stress components are proportional to the applied displacement U and the IERR is proportional to the square applied displacement, which writes:

$$\begin{cases} \sigma_{\mathrm{nn}}(S) = k(S)\frac{E}{1-\nu^2}\frac{U}{W} \geqslant \sigma_{\mathrm{c}}, \\ \mathcal{G}_{\mathrm{inc}}(S) = A(S)\frac{E}{1-\nu^2}W\left(\frac{U}{W}\right)^2 \geqslant G_c. \end{cases} \tag{4}$$

The dimensionless functions k and A are obtained by finite element (FE) calculations for different crack surfaces, as detailed in next section, W is the specimen width, E and ν are the $\vec{a}$-axis direction Young's modulus and Poisson's ratio. The coupling of both conditions reverts in determining the minimum imposed displacement U_{c} for which both conditions are simultaneously fulfilled. For monotonic variations of the stress and of the IERR, the crack surface at initiation S_{c} is determined by combining the two equalities given in Equation (4) and solving the following equation:

$$\frac{A(S_{\mathrm{c}})}{k(S_{\mathrm{c}})^2} = \frac{\ell_{\mathrm{mat}}}{W} \tag{5}$$

Then, the initiation imposed displacement U_{c} is deduced from Equation (4) as:

$$U_{\mathrm{c}} = \frac{W\sigma_{\mathrm{c}}}{Ek(S_{\mathrm{c}})} = \sqrt{\frac{W\mathcal{G}_{\mathrm{c}}}{EA(S_{\mathrm{c}})}} \tag{6}$$

The CC thus takes as input the material elastic and fracture properties, and yields as outputs the initiation imposed displacement and crack surface.

3.2 Numerical simulation

The CC is implemented through FE calculations (Abaqus quasi-static implicit solver) of the stress and of the IERR. The FE calculations are performed under linear elasticity and assuming small deformations. The mesh consists of quadratic tetrahedra with 10 nodes and 4 integration points. It is refined near the defect on the crack plane (minimum mesh size of 0.3 µm) and typically has around 1.5 M degrees of freedom, which results in differences in the initiation displacement smaller than 1 % for a finer mesh. Dirichlet boundary conditions are imposed at the span and support locations to replicate the bending loading. The anisotropic elastic properties, taken from the literature, are C_{11} =466 GPa, C_{12} =117 GPa, C_{13} =127 GPa, C_{22} =506 GPa, C_{36} =94 GPa, C_{44} =235 GPa, where C is the stiffness matrix in Voigt's notation. The stiffness matrix is defined in the material local axis system that corresponds to the global axis system $(O, \vec{x}, \vec{y}, \vec{z})$, *i.e.,* the $\vec{a}$-axis is along $(O\vec{x})$ and the $\vec{c}$-axis is along $(O\vec{y})$. A first calculation without crack is performed in order to determine the stress fields on the crack plane around the defect. This step enables computing the stress isocontours and thus the function k (see Section 3.1). An example of crack shapes based on the stress field isocontours is depicted in Figure 2(b). Once the crack shapes are defined, the lines corresponding to their crack fronts are included in the specimen geometry so that the mesh follows the crack front shapes. This is of practical importance for the calculation of the elastic strain energy variation as a function of the crack surface. Indeed, the elastic strain energy is calculated by successively unbuttoning the nodes lying on the surfaces delimited by the stress isocontour lines. This step allows computing the IERR and thus the function A as a function of the crack surface.

The IERR variation as a function of the normalized crack surface is shown in Figure 3 for different edge defect depths up to 40 µm (symbols in Figure 3) and compared to the case without defect (solid line in Figure 3). The overall increasing trend as a function of the crack

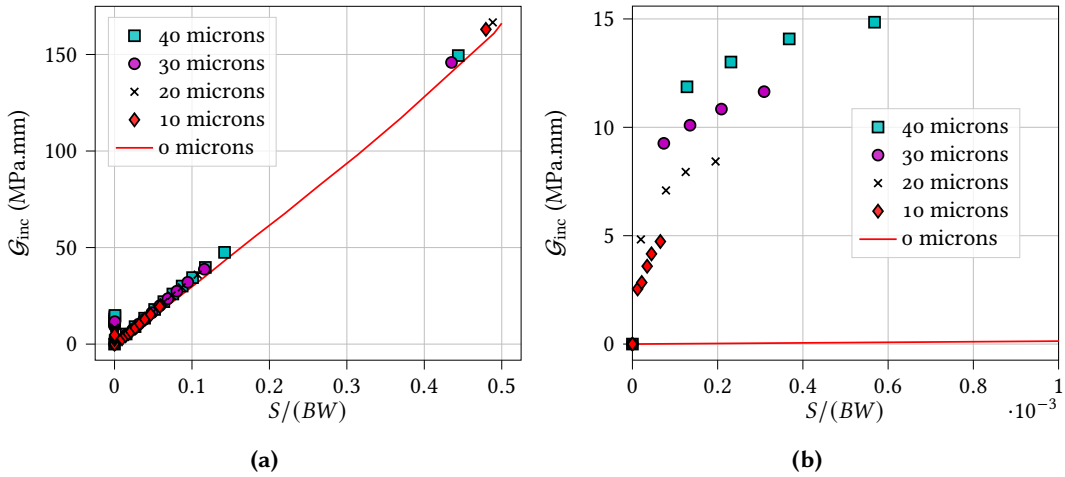

Figure 3: a) IERR as a function of the normalized crack surface obtained for several edge defect depths. b) Focus on small normalized crack surfaces for which the IERR increases with increasing defect size compared to the case without defect.

surface is retrieved whatever the edge defect depth, so that the IERR variation is similar for large enough normalized crack surfaces whatever the defect depth (Figure 3(a)). However, significant differences arise for small crack surfaces as the larger the defect depth, the larger the IERR (Figure 3(b)). It can also be noted that the larger the defect depth, the larger the zone over which the IERR in presence of a defect significantly increases compared to the case without defect. After the initial increase corresponding to the influence of the edge defect, the IERR slightly decreases as the crack surface spans the whole specimen width to retrieve a similar value as in the case without defect. As a consequence, it can be expected that the initiation loading significantly decreases if the initiation surface is small enough whereas if the crack surface at initiation is sufficiently large, the IERR remains the same as in the case without defect.

The variation of the stress normal to the crack plane before initiation is shown in Figure 4. Whatever the defect depth, there is a decreasing stress variation as a function of the normalized

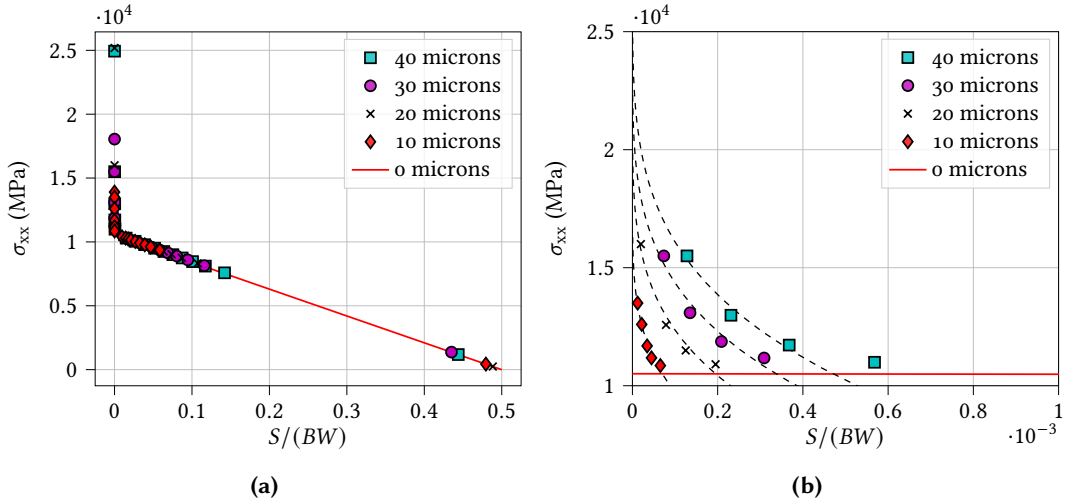

Figure 4: a) Opening stress as a function of the normalized crack surface obtained for several edge defect depths. b) Focus on small normalized crack surfaces for which the stress increases with increasing defect size compared to the case without defect.

crack surface, with similar values for sufficiently large crack surfaces whatever the defect depth Figure 4(a). However, when approaching the defect location, the stress becomes significantly larger than in the case without defect. Indeed, without defect, the stress variation has a linear trend up to the maximum value corresponding to the bending strength for the imposed initiation displacement. The presence of a defect induces a singularity which makes the stress theoretically tend towards infinity when approaching the defect location (Figure 4(b)) (Leguillon et al. 1987; Carpinteri 1987). The larger the defect depth, the larger the stress locally and the larger the zone over which the stress is higher than in the case without defect. It means that similarly to the analysis about the IERR, it can be expected that the initiation loading remains similar to the case without defect if the crack surface at initiation is sufficiently large, and that a smaller initiation loading is obtained for sufficiently small crack surfaces at initiation.

4 Sapphire fracture under bending

We now study the influence of the edge defect depth on the initiation imposed displacement and resulting bending strength. It is observed from Equation (5) that for a given specimen geometry and defect depth, the crack surface at initiation only depends on the Irwin's length. The imposed displacement required for crack initiation is shown as a function of the normalized Irwin's length in Figure 5(a). As expected from the analysis of the stress and of the IERR in the previous section,

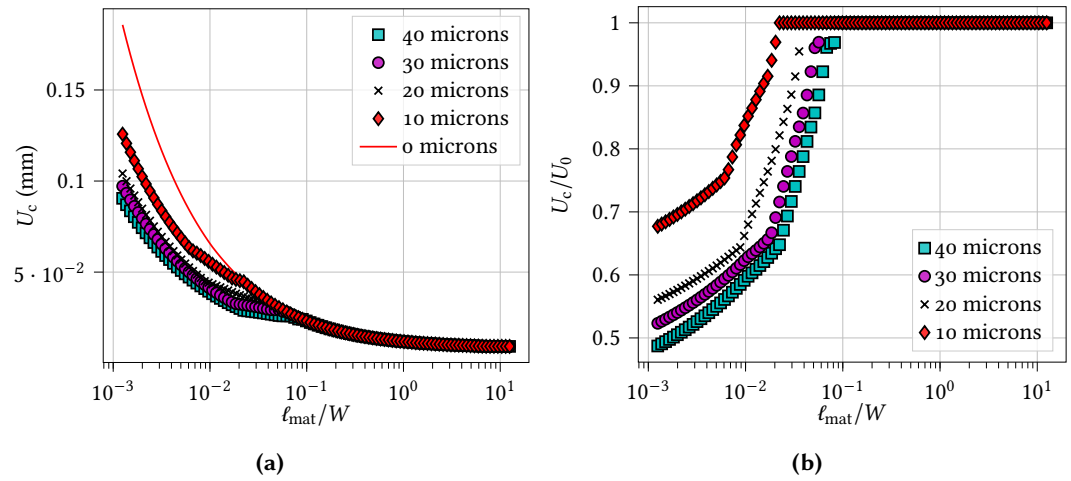

Figure 5: a) Imposed displacement at crack initiation (U_c) and b) ratio between the imposed displacements at crack initiation with (U_c) and without defect (U_0) as a function of Irwin's length to specimen width ratio for different defect depths.

for a given defect depth, the imposed displacement at crack initiation is the same as the one without defect provided that Irwin's length is large enough. It means that materials exhibiting larger Irwin's length are more tolerant to the presence of large defects, and vice-versa. For smaller Irwin's length, the influence of the defect is significant as it induces a decrease in the imposed displacement at initiation, which is smaller for larger defect depths. The transition between the two regimes can be evidenced when studying the variation of the ratio between the imposed displacement at initiation in presence of a defect or without it (Figure 5(b)). The same imposed displacement at initiation is obtained for sufficiently large Irwin's length, whereas the ratio of the initiation displacement decreases with decreasing Irwin's length. The transition between both situations happens for $\ell_{\text{mat}} \approx 2d$. It means that if the Irwin's length is larger than $2d$ (which may happen, *e.g.,* if the tensile strength is sufficiently small), it is like there was no edge defect in the material, *i.e.,* the defect size is too small to induce a decrease in the bending strength.
We finally analyze the bending strength decrease with increasing defect depth obtained using the CC and compare it to the experimental measurements presented in Section 2. Figure 6 shows the bending strength to tensile strength variation as a function of the defect depth for $\sigma_c = 750$ MPa (Figure 6(a)) or $\sigma_c = 850$ MPa (Figure 6(b)) and different Irwin's lengths. If the

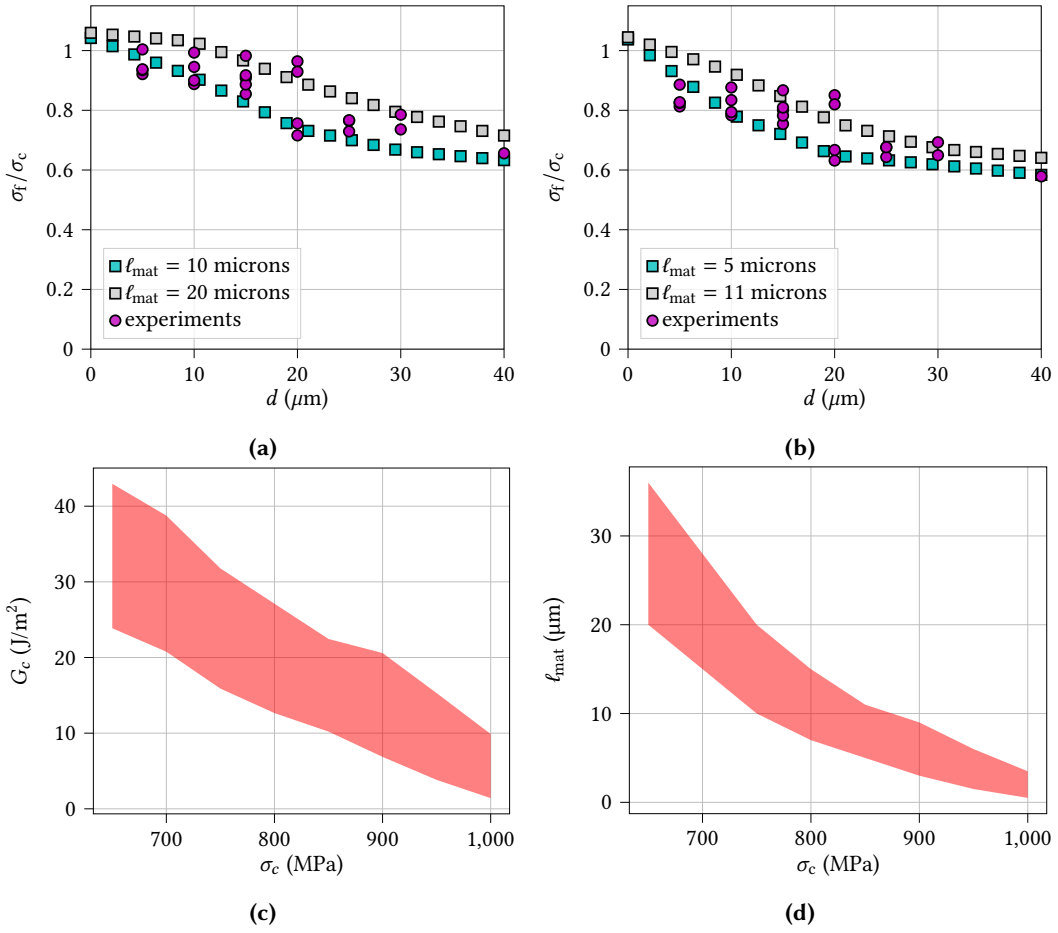

Figure 6: a-b) Bending strength (σ_f) to tensile strength (σ_c) ratio as a function of the defect depth (d) for two Irwin's lengths and a) $\sigma_c = 750$ MPa, b) $\sigma_c = 850$ MPa. Tensile strengths and c) Critical ERR or d) Irwin's length couples that well represent the bending strength decrease as a function of the defect depth.

Irwin's length is smaller than 10 µm (for $\sigma_c = 750$ MPa, Figure 6(a)) or than 5 µm (for $\sigma_c = 850$ MPa, Figure 6(b)), the decrease in bending strength predicted by the CC is too severe compared to the one measured experimentally. On the contrary, if the Irwin's length is larger than 20 µm (for $\sigma_c = 750$ MPa, Figure 6(a)) or 11 µm (for $\sigma_c = 850$ MPa, Figure 6(b)), the obtained bending strength variation overestimates the experimental measurements. For Irwin's length between 10 µm and 20 µm (Figure 6(a)) or between 5 µm and 11 µm (Figure 6(b)) , the model provides a reasonably good representation of the bending strength variation measured experimentally. For a given tensile strength, it is thus possible to determine the critical ERR range for which the

failure stresses obtained with the model lies within the range measured experimentally. It yields $15\,\mathrm{J\,m^{-2}} \leqslant \mathcal{G}_c \leqslant 30\,\mathrm{J\,m^{-2}}$ for $\sigma_c = 750\,\mathrm{MPa}$ and $10\,\mathrm{J\,m^{-2}} \leqslant \mathcal{G}_c \leqslant 22\,\mathrm{J\,m^{-2}}$ for $\sigma_c = 850\,\mathrm{MPa}$.

This procedure can be repeated for other values of σ_c, which yields the admissible couples of tensile strengths and critical ERR (or equivalently, Irwin's length) for the studied material. They are represented in Figures 6(c) and 6(d). It can be noted that for $\sigma_c \leqslant 650\,\mathrm{MPa}$, the bending strength variation is not well captured. In general, the ceramic critical ERR can be determined based on notched bending tests (Ozcoban et al. 2010; García-Prieto et al. 2012; Schlacher et al. 2023) or indentation tests (Quinn et al. 1997; Haney et al. 2011; Henry et al. 2022) for instance. The proposed approach thus enables determining the corresponding tensile strength. For instance, considering a critical ERR $\mathcal{G}_c = 20\,\mathrm{J\,m^{-2}}$ (Doitrand et al. 2020a) yields a corresponding tensile strength of $\sigma_c = 805 \pm 90\,\mathrm{MPa}$. Considering a 2.32 $\mathrm{MPa.\sqrt{m}}$ a-plane critical stress intensity factor (Huang et al. 2021), which corresponds to $\mathcal{G}_c = 15\,\mathrm{J\,m^{-2}}$, it yields a sapphire a-plane tensile strength of $\sigma_c = 850 \pm 90\,\mathrm{MPa}$.

Considering the edge defect-induced crack initiation, the proposed approach is able to explain the overall scattering level measured experimentally on this batch of specimens. For a given Irwin's length and tensile strength, the proposed model provides a single value of the bending strength whereas there is also a certain scattering in the experimental measurements for a given defect depth. This may be due to the fact that the defect shape slightly varies depending on the specimen, whereas a single shape is considered in the proposed model. The defect shape may thus also have an influence on the bending strength (Leguillon et al. 2018; Martin et al. 2018; Doitrand et al. 2020a), nevertheless it seems to be a second order parameter when compared to the defect size.

5 Conclusion

Bending tests on mirror-polished millimetric sapphire specimens with $\vec{a}$-axis oriented along the specimen length reveal that the scattering in the measured bending strength is mainly due to edge defects of some tens of microns resulting from the specimen cutting process. The larger the defect, the smaller the bending strength, which may also slightly depend on the defect shape. Crack initiation occurs from an edge defect along a specimen a-plane before deviating along weaker m-planes that favour further crack propagation. The coupled criterion shows that the sensitivity of the material to edge defect-induced crack initiation mainly depends on Irwin's length. For Irwin's lengths larger than twice the defect depth, the bending strength is the same as the one obtained without defect. For smaller Irwin's lengths, the decrease in the bending strength compared to the case without defect is more pronounced for larger defects. In the present experiments, the sapphire Irwin's length is sufficiently small so that the material is sensitive to the defects, which explains the bending strength decrease with increasing defect size. For a given tensile strength, the comparison between the bending strength decrease with increasing defect depth obtained experimentally and numerically enables determining a range of material critical ERR. Conversely, based on the knowledge of the material critical ERR, the proposed approach yield an indirect way of determining the ceramic a-plane tensile strength, which turns to be evaluated as $850 \pm 90\,\mathrm{MPa}$ for the sapphire under investigation.

References

Barenblatt, G. (1959). "The formation of equilibrium cracks during brittle fracture. General ideas and hypotheses. Axially-symmetric cracks". *Journal of Applied Mathematics and Mechanics* 23.3, pp. 622–636. DOI: 10.1016/0021-8928(59)90157-1

Burhan, M., T. Scalici, Z. Ullah, Z. Kazanc, and G. Catalanotti (2024). "A three-dimensional Finite Fracture Mechanics model to predict free edge delamination in angle-ply laminates". *Engineering Fracture Mechanics* 306, p. 110156. DOI: https://doi.org/10.1016/j.engfracmech.2024.110156

Carpinteri, A. (1987). "Stress-singularity and generalized fracture toughness at the vertex of re-entrant corners". *Engineering Fracture Mechanics* 26.1, pp. 143–155. DOI: https://doi.org/10.1016/0013-7944(87)90086-5

Carpinteri, A., P. Cornetti, and A. Sapora (2012). "A Finite Fracture Mechanics approach to the asymptotic behaviour of U-notched structures". *Fatigue and Fracture of Engineering Materials and Structures* 35.5, pp. 451–457. DOI: https://doi.org/10.1111/j.1460-2695.2011.01637.x

Carrère, N., A. Doitrand, E. Martin, and D. Leguillon (2021). "Theoretical study based on 2D assumptions of the influence of small pores on crack initiation in adhesively bonded joints". *International Journal of Adhesion and Adhesives* 111, p. 102979. DOI: https://doi.org/10.1016/j.ijadhadh.2021.102979

Chao Correas, A., M. Corrado, A. Sapora, and P. Cornetti (2021). "Size-effect on the apparent tensile strength of brittle materials with spherical cavities". *Theoretical and Applied Fracture Mechanics* 116, p. 103120. DOI: https://doi.org/10.1016/j.tafmec.2021.103120

Cornetti, P., M. Muñoz-Reja, A. Sapora, and A. Carpinteri (2019). "Finite Fracture Mechanics and cohesive crack model: weight functions vs. cohesive laws". *International Journal of Solids and Structures* 156-157, pp. 126–136. DOI: https://doi.org/10.1016/j.ijsolstr.2018.08.003

Cornetti, P., N. Pugno, A. Carpinteri, and D. Taylor (2006). "Finite fracture mechanics: A coupled stress and energy failure criterion". *Engineering Fracture Mechanics* 73.14, pp. 2021–2033. DOI: https://doi.org/10.1016/j.engfracmech.2006.03.010

Doitrand, A., T. Duminy, H. Girard, and X. Chen (2024). "A review of the coupled criterion". DOI: https://hal.science/hal-04023438

Doitrand, A., C. Fagiano, N. Carrére, V. Chiaruttini, and M. Hirsekorn (2017). "Damage onset modeling in woven composites based on a coupled stress and energy criterion". *Engineering Fracture Mechanics* 169, 189–200. DOI: https://doi.org/10.1016/j.engfracmech.2016.11.021

Doitrand, A., R. Henry, J. Chevalier, and S. Meille (2020a). "Revisiting the strength of micron-scale ceramic platelets". *Journal of the American Ceramic Society* 103, 6991– 7000. DOI: https://doi.org/10.1111/jace.17148

Doitrand, A., R. Henry, T. Lube, and S. Meille (2021a). "Size effect assessment by Weibull's approach and the coupled criterion". *Engineering Fracture Mechanics* 256, p. 107979. DOI: https://doi.org/10.1016/j.engfracmech.2021.107979

Doitrand, A., R. Henry, H. Saad, S. Deville, and S. Meille (2020b). "Determination of interface fracture properties by micro- and macro-scale experiments in nacre-like alumina". *Journal of the Mechanics and Physics of Solids* 145, p. 104143. DOI: https://doi.org/10.1016/j.jmps.2020.104143

Doitrand, A. and D. Leguillon (2018). "3D application of the coupled criterion to crack initiation prediction in epoxy/aluminum specimens under four point bending". *International Journal of Solids and Structures* 143, pp. 175–182. DOI: https://doi.org/10.1016/j.ijsolstr.2018.03.005

Doitrand, A. and D. Leguillon (2021b). "Asymptotic analysis of pore crack initiation near a free edge". *Theoretical and Applied Fracture Mechanics* 116, p. 103125. DOI: https://doi.org/10.1016/j.tafmec.2021.103125

Doitrand, A., E. Martin, and D. Leguillon (2020c). "Numerical implementation of the coupled criterion: Matched asymptotic and full finite element approaches". *Finite Element in Analysis and Design* 168, p. 103344. DOI: https://doi.org/10.1016/j.finel.2019.103344

Dugdale, D. (1960). "Yielding of steel sheets containing slits". *Journal of the Mechanics and Physics of Solids* 8.2, pp. 100–104. DOI: 10.1016/0022-5096(60)90013-2

Dunn, M., W. Suwito, and S. Cunningham (1997). "Fracture initiation at sharp notches: Correlation using critical stress intensities". *International Journal of Solids and Structures* 34.29, pp. 3873–3883. DOI: https://doi.org/10.1016/S0020-7683(96)00236-3

Felger, J., N. Stein, and W. Becker (2017). "Asymptotic finite fracture mechanics solution for crack onset at elliptical holes in composite plates of finite-width". *Engineering Fracture Mechanics* 182, pp. 621–634. DOI: https://doi.org/10.1016/j.engfracmech.2017.05.048

Ferrian, F., A. Chao Correas, P. Cornetti, and A. Sapora (2022). "Size effects on spheroidal voids by Finite Fracture Mechanics and application to corrosion pits". *Fatigue & Fracture of Engineering Materials & Structures* n/a.n/a. DOI: https://doi.org/10.1111/ffe.13902

García, I., B. Carter, A. Ingraffea, and V. Mantič (2016). "A numerical study of transverse cracking in cross-ply laminates by 3D finite fracture mechanics". *Composites Part B* 95, pp. 475–487. DOI: https://doi.org/10.1016/j.compositesb.2016.03.023

García, I., V. Mantič, and A. Blázquez (2018). "The effect of residual thermal stresses on transverse cracking in cross-ply laminates: an application of the coupled criterion of the finite fracture mechanics". *International Journal of Fracture* 211, 61–74. DOI: https://doi.org/10.1007/s10704-018-0276-9

García-Prieto, A. and C. Baudín (2012). "Influence of experimental variables on fracture toughness determined on SEVNB in three points bending. Mullite a case study". *Journal of the European Ceramic Society* 32.16, pp. 4241–4248. DOI: https://doi.org/10.1016/j.jeurceramsoc.2012.06.018

Girard, H., A. Doitrand, B. Koohbor, R. Rinaldi, N. Godin, D. Long, and J. Bikard (2024). "Influence of nearby fiber on fiber–matrix debonding: Coupled Criterion prediction and debonding shape determination". *Journal of the Mechanics and Physics of Solids* 183, p. 105498. DOI: https://doi.org/10.1016/j.jmps.2023.105498

Griffith, A. (1921). "The Phenomena of Rupture and Flow in Solids". *Philosophical Transactions of the Royal Society of London A: Mathematical, Physical and Engineering Sciences* 221.582-593, pp. 163–198

Griffith, A. (1924). "The theory of rupture". *First Int. Cong. Appl. Mech*, pp. 55–63

Haney, E. and G. Subhash (2011). "Static and dynamic indentation response of basal and prism plane sapphire". *Journal of the European Ceramic Society* 31.9, pp. 1713–1721. DOI: https://doi.org/10.1016/j.jeurceramsoc.2011.03.006

Hashin, Z. (1996). "Finite thermoelastic fracture criterion with application to laminate cracking analysis". *Journal of the Mechanics and Physics of Solids* 44.7, pp. 1129–1145. DOI: https://doi.org/10.1016/0022-5096(95)00080-1

Henry, R., N. Le Roux, I. Zacharie-Aubrun, J. Gatt, C. Langlois, and S. Meille (2022). "Indentation cracking in mono and polycrystalline cubic zirconia: Methodology of an apparent fracture toughness evaluation". *Materials Science and Engineering: A* 860, p. 144261. DOI: https://doi.org/10.1016/j.msea.2022.144261

Huang, S., J. Lin, N. Wang, B. Guo, F. Jiang, Q. Wen, and X. Lu (2021). "Fracture Behavior of Single-Crystal Sapphire in Different Crystal Orientations". *Crystals* 11.8. DOI: 10.3390/cryst11080930

Irwin, G. R. (1948). *Fracture dynamics*

Irwin, G. (1957). "Analysis of Stresses and Strains Near the End of a Crack Traversing a Plate". *Journal of Applied Mechanics* 24.3, pp. 361–364. DOI: 10.1115/1.4011547

Irwin, G. (1958). *Fracture*. Springer Berlin Heidelberg, 551–590

Jiménez-Alfaro, S. and D. Leguillon (2021). "Finite fracture Mechanics at the micro-scale. Application to bending tests of micro cantilever beams". *Engineering Fracture Mechanics* 258, p. 108012. DOI: https://doi.org/10.1016/j.engfracmech.2021.108012

Labossiere, P. and M. Dunn (1999). "Stress intensities at interface corners in anisotropic bimaterials". *Engineering Fracture Mechanics* 62.6, pp. 555–576. DOI: https://doi.org/10.1016/S0013-7944(99)00005-3

Leguillon, D. (2001). "A criterion for crack nucleation at a notch in homogeneous materials". *Comptes Rendus de l'Académie des Sciences - Series IIB - Mechanics* 329.2, pp. 97–102. DOI: https://doi.org/10.1016/S1620-7742(01)01302-2

Leguillon, D. (2002). "Strength or toughness? A criterion for crack onset at a notch". *European Journal of Mechanics - A/Solids* 21(1), pp. 61–72. DOI: https://doi.org/10.1016/S0997-7538(01)01184-6

Leguillon, D. (2014). "An attempt to extend the 2D coupled criterion for crack nucleation in brittle materials to the 3D case". *Theoretical and Applied Fracture Mechanics* 74, pp. 7–17. DOI: https://doi.org/10.1016/j.tafmec.2014.05.004

Leguillon, D., E. Martin, O. Sevecek, and R. Bermejo (2018). "What is the tensile strength of a ceramic to be used in numerical models for predicting crack initiation?" *International Journal of Fracture* 212, pp. 86–103. DOI: https://doi.org/10.1007/s10704-018-0294-7

Leguillon, D., D. Quesada, C. Putot, and E. Martin (2007). "Prediction of crack initiation at blunt notches and cavities – size effects". *Engineering Fracture Mechanics* 74.15, pp. 2420–2436. DOI: 10.1016/j.engfracmech.2006.11.008

Leguillon, D. and E. Sanchez-Palencia (1987). *Computation of Singular Solutions in Elliptic Problems and Elasticity*. Wiley, USA

Leguillon, D., S. Tariolle, E. Martin, T. Chartier, and J. Besson (2006). "Prediction of crack deflection in porous/dense ceramic laminates". *Journal of the European Ceramic Society* 26.3, pp. 343–349. DOI: https://doi.org/10.1016/j.jeurceramsoc.2004.11.003

Li, J. and X. Zhang (2006). "A criterion study for non-singular stress concentrations in brittle or quasi-brittle materials". *Engineering Fracture Mechanics* 73, pp. 505–523. DOI: https://doi.org/10.1016/j.engfracmech.2005.09.001

Martin, E., D. Leguillon, and N. Carrère (2012). "A coupled strength and toughness criterion for the prediction of the open hole tensile strength of a composite plate". *International Journal of Solids and Structures* 49.26, pp. 3915–3922. DOI: https://doi.org/10.1016/j.ijsolstr.2012.08.020

Martin, E., D. Leguillon, O. Sevecek, and R. Bermejo (2018). "Understanding the tensile strength of ceramics in the presence of small critical flaws". *Engineering Fracture Mechanics* 201, pp. 167–175. DOI: https://doi.org/10.1016/j.engfracmech.2018.06.021

McClintock, F. and G. Irwin (Jan. 1965). "Plasticity Aspects of Fracture Mechanics". *Fracture Toughness Testing and its Applications*. ASTM International. DOI: 10.1520/STP26586S

Molnár, G., A. Doitrand, R. Estevez, and A. Gravouil (2020). "Toughness or strength? Regularization in phase-field fracture explained by the coupled criterion". *Theoretical and Applied Fracture Mechanics* 109, p. 102736. DOI: https://doi.org/10.1016/j.tafmec.2020.102736

Nairn, J. (2000). "Fracture mechanics of composites with residual stresses, traction-loaded cracks, and imperfect interfaces". *Fracture of Polymers, Composites and Adhesives*. Ed. by J. Williams and A. Pavan. Vol. 27. European Structural Integrity Society. Elsevier, pp. 111–121. DOI: https://doi.org/10.1016/S1566-1369(00)80012-6

Nishida, T., Y. Hanaki, and G. Pezzotti (1994). "Effect of Notch-Root Radius on the Fracture Toughness of a Fine-Grained Alumina". *Journal of the American Ceramic Society* 77.2, pp. 606–608. DOI: https://doi.org/10.1111/j.1151-2916.1994.tb07038.x

Orowan, E. (1949). "Fracture and strength of solids". *Reports on Progressin Physics* 12, pp. 185–232

Ozcoban, H, H Jelitto, and G. Schneider (2010). "Influence of finite notch root radius and optically determined crack length on the measured fracture toughness of brittle materials". *Journal of the European Ceramic Society* 30.7, pp. 1579–1583. DOI: https://doi.org/10.1016/j.jeurceramsoc.2010.01.022

Papšík, R., O. Seveček, A. Hofer, I. Kraleva, J. Kreith, and R. Bermejo (2023). "Prediction of edge and tunnelling crack formation in layered ceramics using a stress-energy fracture criterion". *Journal of the European Ceramic Society* 43.7. 17th European Inter-Regional Conference on Ceramics, pp. 2928–2934. DOI: https://doi.org/10.1016/j.jeurceramsoc.2022.12.022

Picard, D., D. Leguillon, and C. Putot (2006). "A method to estimate the influence of the notch-root radius on the fracture toughness measurement of ceramics". *Journal of the European Ceramic Society* 26.8, pp. 1421–1427. DOI: https://doi.org/10.1016/j.jeurceramsoc.2005.02.016

Quinn, G (2020). *NIST Recommended Practice Guide: Fractography of Ceramics and Glasses, 3rd edition*. DOI: https://doi.org/10.6028/NIST.SP.960-16e3

Quinn, J. and G. Quinn (1997). "Indentation brittleness of ceramics: a fresh approach". *Journal of Materials Science* 32.16, pp. 4331–4346. DOI: https://doi.org/10.1023/A:1018671823059

Romani, R., M. Bornert, D. Leguillon, R. Le Roy, and K. Sab (2015). "Detection of crack onset in double cleavage drilled specimens of plaster under compression by digital image correlation - Theoretical predictions based on a coupled criterion". *Eur. J. Mech. A/Sol.* 51, pp. 172–182. DOI: https://doi.org/10.1016/j.euromechsol.2014.12.002

Rosendahl, P., N. Weißgraeber P.and Stein, and W. Becker (2017). "Asymmetric crack onset at open-holes under tensile and in-plane bending loading". *International Journal of Solids and Structures* 113-114, pp. 10–23. DOI: https://doi.org/10.1016/j.ijsolstr.2016.09.011

Sapora, A and P Cornetti (2018). "Crack onset and propagation stability from a circular hole under biaxial loading". *International Journal of Fracture* 214.1, pp. 97–104. DOI: https://doi.org/10.1007/s10704-018-0315-6

Sapora, A., P. Cornetti, A. Campagnolo, and G. Meneghetti (2021). "Mode I fatigue limit of notched structures: A deeper insight into Finite Fracture Mechanics". *International Journal of Fracture* 227, pp. 1–13. DOI: https://doi.org/10.1007/s10704-020-00488-6

Schlacher, J., T. Csanádi, T. Vojtko, R. Papšík, and R. Bermejo (2023). "Micro-scale fracture toughness of textured alumina ceramics". *Journal of the European Ceramic Society* 43.7. 17th European Inter-Regional Conference on Ceramics, pp. 2943–2950. DOI: https://doi.org/10.1016/j.jeurceramsoc.2022.06.028

Sevecek, O., J. Hanak, Z. Majer, D. Drdlik, Z. Chlup, and M. Kotoul (2019). "Prediction of the Ceramic Foam Structure Failure Using a Detailed Finite Element Model". *Key Engineering Materials* 827, 222–7. DOI: http://dx.doi.org/10.1016/j.engfracmech.2014.07.031

Taylor, D. (2007). *The Theory of Critical Distances*. Oxford: Elsevier Science Ltd

Uhl, J., A. Doitrand, and S. Meille (2022). "Variability in porous ceramic fracture: Influence of apparent density and critical pores". *Journal of the European Ceramic Society*. DOI: https://doi.org/10.1016/j.jeurceramsoc.2022.05.020

Vereecke, J., C. Bois, J. Wahl, T. Briand, L. Ballère, and F. Lavelle (2024). "Explicit modelling of meso-scale damage in laminated composites – Comparison between finite fracture mechanics and cohesive zone model". *Composites Science and Technology* 253, p. 110640. DOI: https://doi.org/10.1016/j.compscitech.2024.110640

Weißgraeber, P., D. Leguillon, and W. Becker (2016a). "A review of Finite Fracture Mechanics: crack initiation at singular and non-singular stress raisers". *Archive Appl. Mech.* 86(1-2), 375–401. DOI: 10.1007/s00419-015-1091-7

Weißgraeber, P., D. Leguillon, and W. Becker (2016b). "Cracks at elliptical holes: Stress intensity factor and Finite Fracture Mechanics solution". *Eur. J. Mech. A/Sol.* 55, pp. 192–198. DOI: http://dx.doi.org/10.1016/j.euromechsol.2015.09.002

Wiederhorn, S. (1969). "Fracture of Sapphire". *Journal of the American Ceramic Society* 52.9, pp. 485–491. DOI: https://doi.org/10.1111/j.1151-2916.1969.tb09199.x

Yosibash, Z. and B. Mittelman (2016). "A 3-D failure initiation criterion from a sharp V-notch edge in elastic brittle structures". *European Journal of Mechanics - A/Solids* 60, pp. 70–94. DOI: https://doi.org/10.1016/j.euromechsol.2016.06.003

Yosibash, Z., E. Priel, and D Leguillon (2006). "A failure criterion for brittle elastic materials under mixed-mode loading". *International Journal of Fracture* 141, 291–312. DOI: https://doi.org/10.1007/s10704-006-0083-6

Authors' contributions SM performed the mechanical tests, AD performed the fracture surface observations, numerical simulations and drafted the manuscript. SM, RH and AD developed the methodology, conceived of the study, and participated in its design, coordination, and critical review of the manuscript. All authors read and approved the final manuscript.